Journal of Environmental Chemical Engineering 5 (2017) 4185–4193

Contents lists available at ScienceDirect

Journal of Environmental Chemical Engineering

journal homepage: www.elsevier.com/locate/jece

Research Paper

# Sodium rhodizonate induced formation of gold nanoparticles supported on cellulose fibers for catalytic reduction of 4-nitrophenol and organic dyes

Md. Tariqul Islam[a], Noemi Dominguez[b], Md. Ariful Ahsan[a], Homero Dominguez-Cisneros[a], Pamela Zuniga[c], Pedro J.J. Alvarez[c], Juan C. Noveron[a,*]

[a] Department of Chemistry, University of Texas at El Paso, 500 West University Avenue, El Paso, TX 79968, USA
[b] Metallurgical and Materials Engineering, University of Texas at El Paso, 500 West University Avenue, El Paso, TX 79968, USA
[c] Civil and Environmental Engineering, Rice University, 6100 Main Street, Houston, TX 77005, USA

ARTICLE INFO

*Keywords:*
Gold nanoparticles
Sodium rhodizonate
Cellulose fibers
Catalytic reduction
4-nitrophenol
Methyl orange
Methylene blue

ABSTRACT

We demonstrate sodium rhodizonate as a novel dual-functional reducing and stabilizing agent to form gold nanoparticles (AuNPs) of controlled size based on temperature. At room temperature (ca. 23 °C), the method generates AuNPs with an average size of ~11 nm, whereas at 80 °C, it forms AuNPs with an average size of ~7 nm. The rhodizonate-stabilized AuNPs readily bind to cellulose fibers (CF) while maintaining a high catalytic activity. The catalytic activity of the CF-supported AuNPs nanocomposites is demonstrated by the reduction of 4-nitrophenol (4-NP) and organic dyes such as methyl orange (MO), methylene blue (MB) in water. A glass column-based continuous catalytic reduction and its recyclability is also demonstrated for practical applications.

## 1. Introduction

A major class of anthropogenic organic pollutants consists of dyes, which are widely used by numerous industries [1–3]. However, a large portion of these dyes is discharged into the environment, which is the key reason for the contamination of water by dyes [4–6]. Like other organic pollutants, many dyes are well known to be toxic, carcinogenic and mutagenic to human beings and aquatic organisms [7–9]. Moreover, many of these dyes are fairly stable and persistent in nature and thereby show resistance to natural degradation [10]. Organic dyes also have high molar absorption coefficient and thereby, can intensely colorize large amount of water, which is undesirable for municipal usage purposes. Therefore, the removal of organic dyes is an indispensible part of wastewater treatment.

Commonly employed methods for the treatment of organic pollutants from wastewater includes, but not limited to, adsorption [11], chemical precipitation [12], photocatalytic degradation [13,14], advanced oxidation processes [15], gamma irradiation [16], and the biological treatment [17]. Removal of organic pollutants by adsorption and chemical precipitation does not destroy them rather transfer the pollutants from one phase to another. Photocatalytic degradation, on the other hand, can degrade organic pollutants to mineralization. However, the requirement of ultraviolet light, low quantum yield and slow rate of degradation limit their practical applicability. Biological treatments can also efficiently decompose the organic compounds using microorganisms such as algae, fungi, bacteria and yeasts. However, some organic pollutants are highly resistant, toxic, and carcinogenic to microorganisms and that is why the typical biological treatment is practically ineffective in their decomposition [18–20]. In this context, catalytic reductive degradation of organic pollutants has been reported as a relatively new and effective method of wastewater treatment technology [21,22]. Catalytic reduction can effectively degrade organic pollutants at a faster rate with better stability and recyclability [5,23]. Moreover, it has been reported that some pollutants in their reduced form become less toxic and thereby can be degraded by biological treatment [24]. As for example, 4-nitrophenol (4-NP), which is a common industrial pollutant can be reduced into less toxic 4-aminophenol (4-AP) [24]. Therefore, chemical reduction followed by biological treatment could be an effective method for the degradation of toxic and carcinogenic organic pollutants from water [25]. In addition, the reduced form of some pollutants *viz.* 4-AP also has industrial applications as a photographic developer, corrosion inhibitor, antioxidant, precursor for the manufacture of analgesic and antipyretic drugs, an intermediate in the synthesis of paracetamol [26,27], etc. Hence, the reduction of organic pollutants is an effective method not only in the context of pollutants treatment, but also is an effective way of resources regeneration.

Most widely used catalysts for the reductive degradation of organic pollutants are based on noble and transition metals [28–30]. Moreover, owing to the high surface area, fast reactivity, recyclability, chemical

* Corresponding author.
*E-mail addresses:* mtislam@miners.utep.edu (Md. T. Islam), jcnoveron@utep.edu (J.C. Noveron).

http://dx.doi.org/10.1016/j.jece.2017.08.017
Received 21 April 2017; Received in revised form 24 July 2017; Accepted 13 August 2017
Available online 18 August 2017
2213-3437/ 

and physical robustness supported noble metal nanoparticles based catalysts are of the prime choice [31,32]. Catalyst supports not only prevent the aggregation of nanoparticles but also often provide high-surface area and facilitate the easier handling, recovery and reuse. This eventually prevents the environmental pollution caused by the leaching of nanoparticles and minimizes the cost at the same time.

Herein, we report a novel method of generating AuNPs that are reduced and stabilized by sodium rhodizonate. The AuNPs readily bind to cellulose fibers (CF) and exhibit effective catalytic properties for the reduction of 4-NP, MO, and MB in deionized as well as tap water. The CF-supported AuNPs catalysts provide convenience in handling, recovery, and reuse. In order to investigate the potential practical application and the stability of the CF-supported AuNPs, a glass column was packed with this nanocomposites and used for continuous catalytic reduction of 4-NP, MO and MB. The packed glass column efficiently reduced 4-NP, MO and MB to their corresponding reduced species for multiple cycles without losing the activity.

## 2. Materials and methods

### 2.1. Materials

Sodium rhodizonate dibasic (97%), hydrogen tetrachloroaurate trihydrate ($HAuCl_4{\cdot}3H_2O$, 99.9%), 4-nitrophenol ($O_2NC_6H_4OH \geq 99\%$), sodium borohydride ($NaBH_4$, 99%), methyl orange (MO), methylene blue (MB) and fibrous cellulose were purchased from Sigma-Aldrich, USA. Sand was purchased from J.T. Baker (part no. 3382-01). Deionized water was obtained from Milli-Q (Advantage A-10) water filter system (resistance > 18.20 MΩ cm) and the tap water was obtained from the regular water line of the lab.

### 2.2. Synthesis of AuNPs

In typical synthesis, to a 100 ml round-bottomed flask containing 20 ml of 0.5 mM solution of $HAuCl_4$ 4 ml of 9.7 mM sodium rhodizonate solution was added, all at once, while stirring vigorously. After few seconds of stirring the reaction mixture turned into a deep burgundy color (Scheme 1), which indicated the formation of AuNPs. After 5 min of stirring the AuNPs solution was preserved under ambient conditions for further characterization, application, and attachment with CF. The AuNPs synthesized at room temperature (ca. RT = 23 °C) are hereafter denoted as AuNPs-RT.

In order to synthesize AuNPs at 80 °C both of the solutions were preheated to 80 °C before mixing. The AuNPs synthesized at 80 °C are hereafter denoted as AuNPs-80C. The concentration of $Au^0$ in the as-prepared AuNPs stock solutions is 0.0821 mg of $Au^0$ per 1 ml of solution.

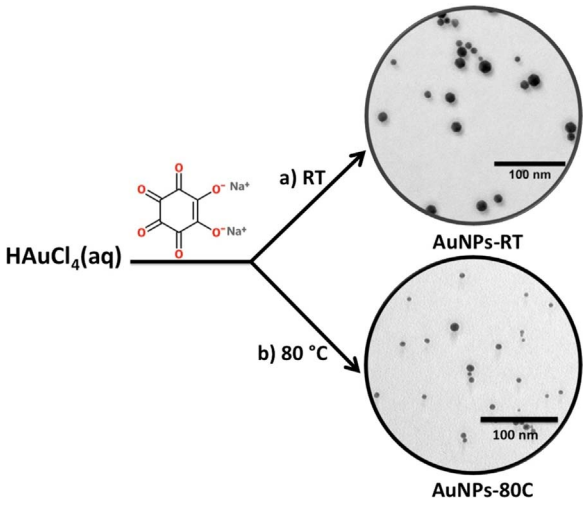


**Scheme 1.** Synthesis of AuNPs reduced and stabilized by sodium rhodizonate at a) room temperature (23 °C) and b) 80 °C.

### 2.3. Preparation of cellulose fibers-supported AuNPs

The AuNPs-RT was used for making the nanocomposites with CF. The nanocomposites are referred to as CF-AuNPs-2.87 and CF-AuNPs-0.98, where the values 2.87 and 0.98 represent the percentage weight of AuNPs loaded on the CF. Two different nanocomposites were prepared differing on the percentage of AuNPs loading and used to investigate the dependence of the rate of reduction on the amount of AuNPs loading. Different quantities of AuNPs-RT stock solution and CF were used depending upon the weight percentage of gold loading. For example, to prepare nanocomposite CF-AuNPs-2.87, 200 mg of CF were added to 72 ml stock solution of AuNPs-RT. This mixture was then bath sonicated for 10 min, which caused AuNPs-RT to bind with the CF, Scheme 2.

The CF bound AuNPs-RT was then separated by centrifugation at a speed of 4000 rpm for 5 min. The centrifuged supernatant showed no plasmonic absorption band centered at 519 nm, which indicates that the AuNPs-RT were attached onto the CF with 100 percent loading efficiency (Supporting information, Fig. S1). The centrifuged nanocomposites were washed repeatedly with DI water and eventually dried in a vacuum oven at 60 °C for overnight. In order to prepare nanocomposite CF-AuNPs-0.98, 200 mg of CF were added to 24 ml of AuNPs-RT stock solution and the aforementioned procedure was followed.

### 2.4. Catalytic reduction of 4-NP, MO and MB by the nanocomposites

The catalytic reductions were carried out in both the deionized as well as tap water following the same experimental procedure. In details, in a standard quartz cuvette, 3 mg of either CF-AuNPs-2.87 or CF-AuNPs-0.98 was added to 2.5 ml of 4-NP aqueous solution (1 mM), followed by the mixture was bath sonicated for 2 min to obtain uniform dispersion throughout. Afterwards, 1 ml of freshly prepared $NaBH_4$ aqueous solution (0.159 M) was added and mixed quickly. The reduction reaction course was monitored by using the kinetics software of the UV–vis spectrophotometer, which monitored the lowering of the absorbance of 4-nitrophenolate at 400 nm in a certain interval of time. It is noteworthy to mention that the 4-NP reacts with $NaBH_4$ to yield 4-nitrophenolate, which shows strong absorption band centered at 400 nm [33,34].

In the reduction of MO and MB, 2 mg of either CF-AuNPs-2.87 or CF-AuNPs-0.98 was added with 10 ml of MO or MB having a concentration of 0.15275 mM (50 ppm) and 0.1563 mM (50 ppm), respectively. The mixture was bath sonicated for about 2 min. Afterwards, 50 mg (1.3217 mmol) $NaBH_4$ powder was quickly added into the above mixture and the reduction reaction course was monitored by the gradual decrease of the absorbance at 465 and 615 nm for the MO and MB, respectively. In order to investigate the adsorption ability of the nanocomposites control experiments were carried out, which showed no adsorption of either 4-NP, MO, or MB on the nanocomposites (Supporting information, Fig. S2).

The time-dependent percent reduction of 4-NP, MO, and MB was calculated using the following equation.

$$\text{Percent reduction} = \frac{A_0 - A_t}{A_0} \times 100\%$$

where $A_0$ and $A_t$ represent the absorbance of 4-NP, MO and MB at the beginning and at time (t) of the catalytic reduction.

### 2.5. Preparation of column reactor for the continuous catalytic reduction

A glass column was packed with the CF-supported AuNPs mixed

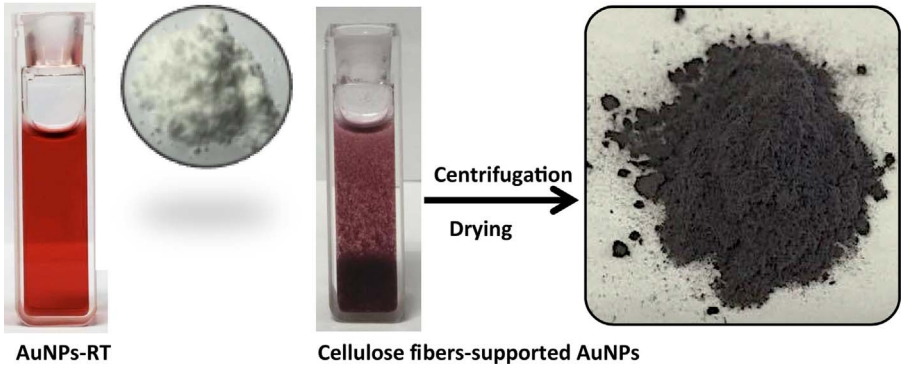


**Scheme 2.** Preparation of CF-supported AuNPs.

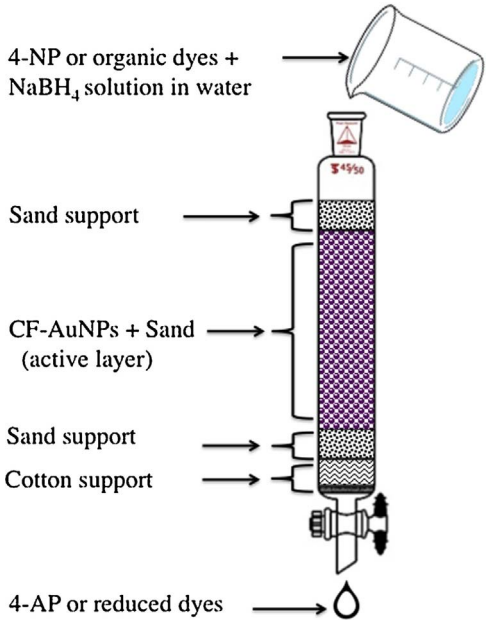


**Scheme 3.** Composition of the column reactor packed with CF-AuNPs and sand for the continuous catalytic reduction of 4-NP, MO, and MB.

with sand and used for continuous catalytic reduction of 4-NP, MO, and MB. The glass chromatographic column having dimensions I.D. × O.D × L = 20 × 26 × 457 mm was used and it was packed about 17.2 cm, Scheme 3.

In detail, 20 ml of AuNPs-RT stock solution (0.0821 mg AuNPs/ml) was mixed with 2 g of CF by bath sonication for about 10 min. The AuNPs-RT bound to the CF was homogeneously mixed with 90 g of sea sand. Afterwards, the column was filled, by wet method, with cotton and coarse sea sand supports at the bottom of the column. The top of the column was also filled with coarse sea sand for about 4 cm. The column was first washed with 500 ml of DI water before running the reduction cycles.

For the continuous catalytic reduction of 4-NP, 120 mg of $NaBH_4$ (3.1721 mmol) powder was dissolved in 50 ml of 1 mM 4-NP solution. The fresh solution was then continuously fed into the column and an average flow of ~ 0.86 ml/min was observed. However, in the continuous reduction of dyes, 50 ml solution of each dye having the concentration of 50 ppm was used. Afterwards, 250 mg of $NaBH_4$ (6.6085 mmol) powder was dissolved in the dye solution and the freshly prepared solution was fed into the column continuously. UV–vis spectra was taken on the feed and eluted solutions to calculate the percent reduction of 4-NP, MO, and MB.

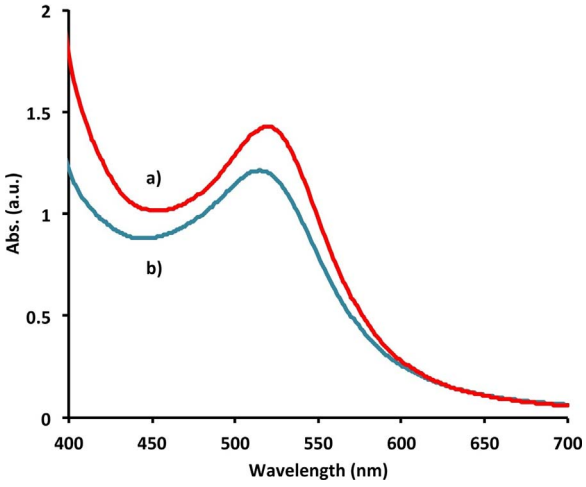


**Fig. 1.** UV–vis absorption spectrum of a) AuNPs-RT and b) AuNPs-80C.

## 3. Characterization of AuNPs and its nanocomposites

### 3.1. UV–visible spectroscopy of the AuNPs

Fig. 1 shows the UV–vis spectrum of the AuNPs-RT and AuNPs-80C stock solutions in water. Strong plasmonic absorption bands centered at 519 nm and 514 nm were observed for the AuNPs-RT and AuNPs-80C, respectively.

It was observed that the plasmonic absorption band generated by AuNPs-RT was about 5 nm red shifted compared to the AuNPs-80C. This red shift in plasmonic absorption band of the AuNPs-RT happened because of the relatively bigger size of the AuNPs-RT compared to the AuNPs-80C.

### 3.2. Transmission electron microscopy (TEM) and energy dispersive X-ray (EDX) of the AuNPs

The typical TEM images of AuNPs with the corresponding size distribution histogram are shown in Fig. 2. TEM images show that the AuNPs are fairly spherical and well dispersed in solution with some aggregations. The corresponding size distribution histogram, Fig. 2c, shows that the AuNPs-RT have an average core size of ~11 nm. On the other hand, the AuNPs-80C have an average core size of ~7 nm. The average smaller particles size of the AuNPs-80C compared to the AuNPs-RT is also revealed by the UV–vis experiment.

Energy-dispersive X-ray analysis was conducted on AuNPs-RT to determine the elemental composition of the nanoparticles (Supporting information, Fig. S3). The EDX spectrum shows the presence of a high abundance of gold as well as traces of C and O in the nanoparticles samples. The C and O peaks have originated from the rhodizonate ions that are bound to the AuNPs surfaces, which further indicates that the

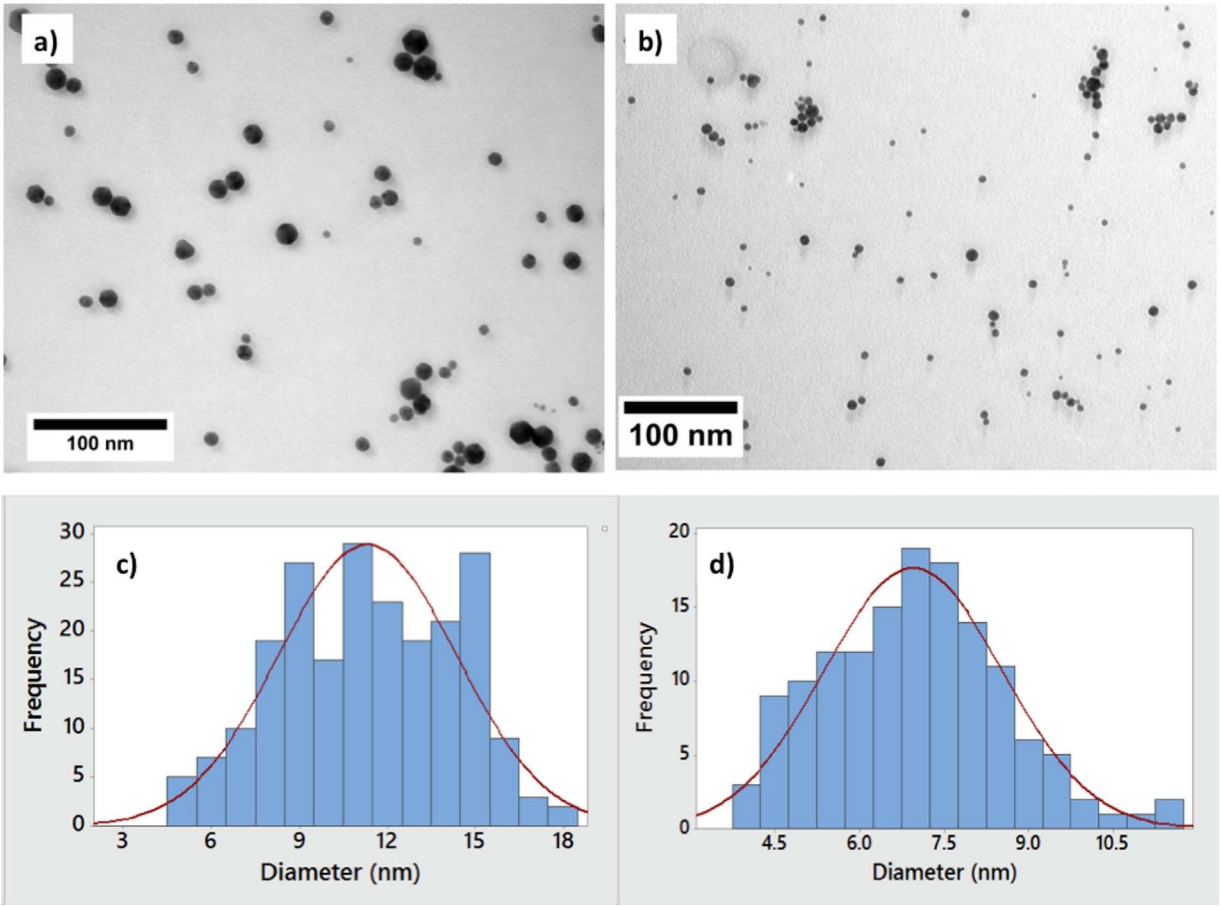


**Fig. 2.** Typical TEM images of a) AuNPs-RT and b) AuNPs-80C. Size distributions of c) AuNPs-RT and d) AuNPs-80C.

AuNPs were stabilized by the excess rhodizonate ions present in the solution. Trace amount of Si and Al is also observed, which originated from mica substrate that was used for the analysis.

### 3.3. Dynamic light scattering and zeta potential measurements of the AuNPs

Dynamic light scattering (DLS) was carried out to determine the size distribution of AuNPs in solution (Supporting information, Fig. S4). The AuNPs-RT exhibited the average hydrodynamic diameter of about 38.88 nm. On the other hand, the AuNPs-80C showed two size distributions *viz.* 14 and 96 nm. These types of size distributions indicate that the AuNPs-80C are dispersed both individually and aggregated in the solution, which was also observed in TEM image (Supporting information, Fig. S5 and S6).

Zeta potential measurements (Supporting information, Fig. S4) showed negative values for both type of the AuNPs. These negative values suggest that the AuNPs surface has a net negative charge, which is due to the binding of rhodizonate molecules on the nanoparticles surface. This also explains the high dispersion stability of the AuNPs in solution due to the interparticles electrostatic repulsive forces.

### 3.4. Transmission electron microscopy (TEM) of the nanocomposites

A typical TEM image of CF-supported AuNPs nanocomposites *viz.* CF-AuNPs-2.87 is shown in Fig. 3. The TEM image shows that AuNPs are distributed all over the CF surfaces. This indicates that the AuNPs certainly have strong affinity for the CF, which caused them to bind together. Similar binding affinity of cellulose towards the noble metal nanoparticles was studied by Junhui et. al. [35] The size distribution of the AuNPs-RT bound to the CF is also shown in the inset.

### 3.5. Scanning electron microscopy (SEM) and EDS of the nanocomposites

Typical SEM image of the CF-AuNPs-2.87 is shown in the inset of Fig. 4 to show the noodles like morphology of the CF. The EDS spectrum performed on CF-AuNPs-2.87 showed the presence of high abundance of carbon, oxygen with relatively lower abundance gold. This further indicates the presence of AuNPs on the CF. In contrary, the pristine CF did not show any gold peak at all in the EDS spectrum (Supporting information, Fig. S7).

### 3.6. X-Ray powder diffraction (XRPD) and BET surface area of the nanocomposites

The X-Ray diffraction patterns of CF-AuNPs-2.87 and CF-AuNPs-0.98 are shown in Fig. 5a and b, respectively. The diffraction peaks located at $2\theta = 14.5^{\circ}$, $16.4^{\circ}$ and $22.4^{\circ}$ corresponds to the 100, 010 and 110 crystalline faces of Iα cellulose, respectively, or the $1\bar{1}0$, 110, and 200 crystalline faces of cellulose Iβ allomorph. These two allomorphs of cellulose usually originate XRD peaks that are located very close to each other. This is why it is difficult to distinguish the cellulose allomorphs from XRD spectrum only. Similar XRD pattern was reported in other researches as well [36,37].

In addition, a set of new diffraction peaks at $37.8^{\circ}$, $43.4^{\circ}$, $64.2^{\circ}$ and $77.4^{\circ}$ was also observed, which corresponds to the 111, 200, 220 and 311 lattice planes of the face-centered cube (fcc) crystalline gold that originated from the AuNPs bound to the CF [38,39]. In addition, it was observed that the relative intensity of the characteristic gold diffraction peaks increased with respect to the increase in AuNPs loading.

The specific surface area of the CF-supported AuNPs was calculated as 100.20, and 155.64 $m^2/g$ for CF-AuNPs-0.98 and CF-AuNPs-2.87,

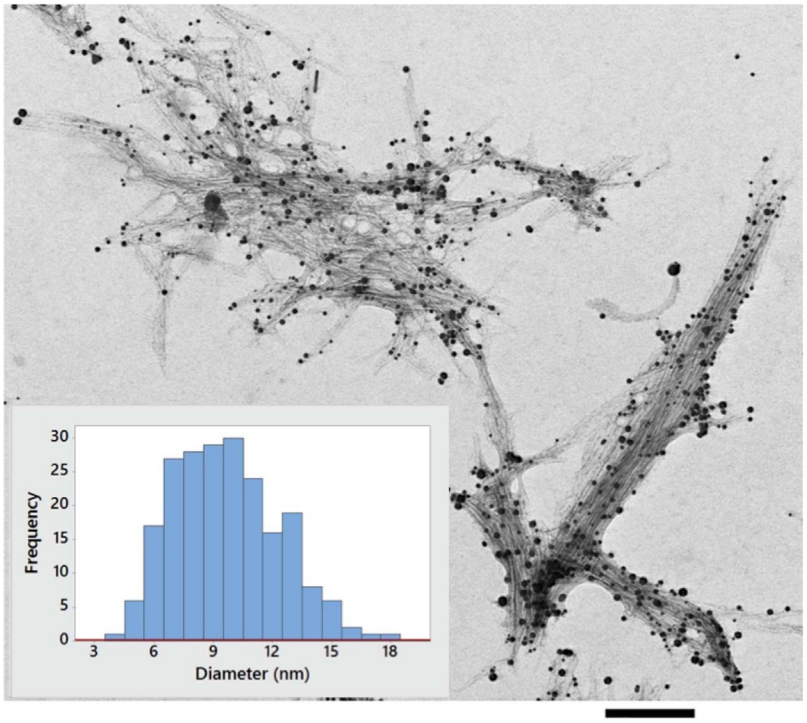


**Fig. 3.** Typical TEM image of CF-AuNPs-2.87 showing the AuNPs bound on the CF. Inset: Size distribution of the AuNPs bound on the CF. Scale bar 200 nm.

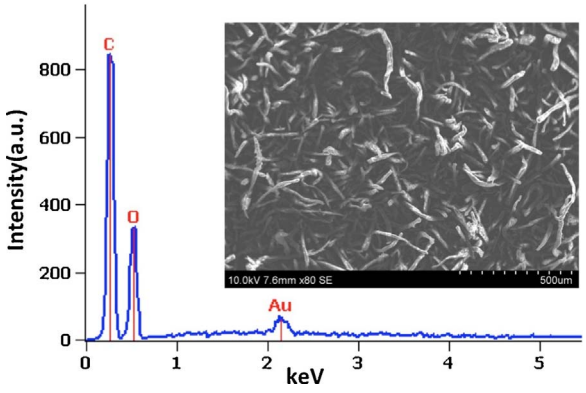


**Fig. 4.** EDX spectrum of the CF-AuNPs-2.87. Inset: SEM images of the CF-AuNPs-2.87.

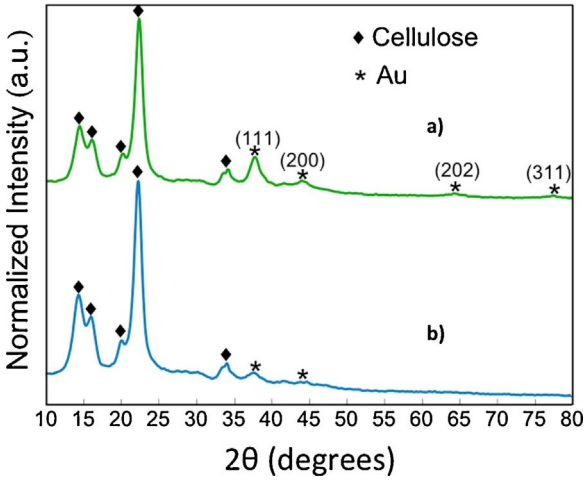


**Fig. 5.** XRD patterns of a) CF-AuNPs-2.87 and b) CF-AuNPs-0.98.

respectively. However, the specific surface area of the pristine CF was calculated as 29.62 $m^2/g$. It was observed that the specific surface area of the nanocomposites increased with the increase in the amount of AuNPs loading.

## 4. Results and discussion

### 4.1. Synthesis of AuNPs and their binding with CF

AuNPs were prepared by mixing $HAuCl_4$ solution with sodium rhodizonate and the reaction generated nanoparticles immediately. At room temperature (ca. 23 °C), this method generated AuNPs with an average size of ~11 nm, whereas at 80 °C, the method formed AuNPs with an average size of ~7 nm. The ability of rhodizonate ion to form coordination complexes with metal ions has been reported before [40,41]. However, the ability of the rhodizonate ion towards the reduction and stabilization of gold ion has not been reported to the best of our knowledge. The AuNPs synthesized at 80 °C had smaller average size compared to the one synthesized at room temperature. One explanation is that the faster rate of the reaction at the higher temperature may form more nucleation sites that in turn lead to the formation of smaller nanoparticles compared to room temperature.

When rhodizonate-stabilized AuNPs are exposed to CF and bath sonicated, they immediately bind to each other with 100 percent AuNPs loading ability. This indicates that the rhodizonate stabilizer is highly labile and exchangeable with the hydroxyl functional groups of CF. In contrast, other AuNPs prepared with the use of stronger stabilizers such as citrate or alkythiols do not readily adsorb on to cellulose, although there are procedures that utilize in-situ formation and binding of AuNPs [42,43].

The catalytic ability of the CF-supported AuNPs towards the reduction of 4-NP, MO, and MB is demonstrated along with the cyclic stability. Moreover, the ability of the nanocomposites towards the continuous catalytic reduction, demonstrated here, may render application in industry as well as water remediation.

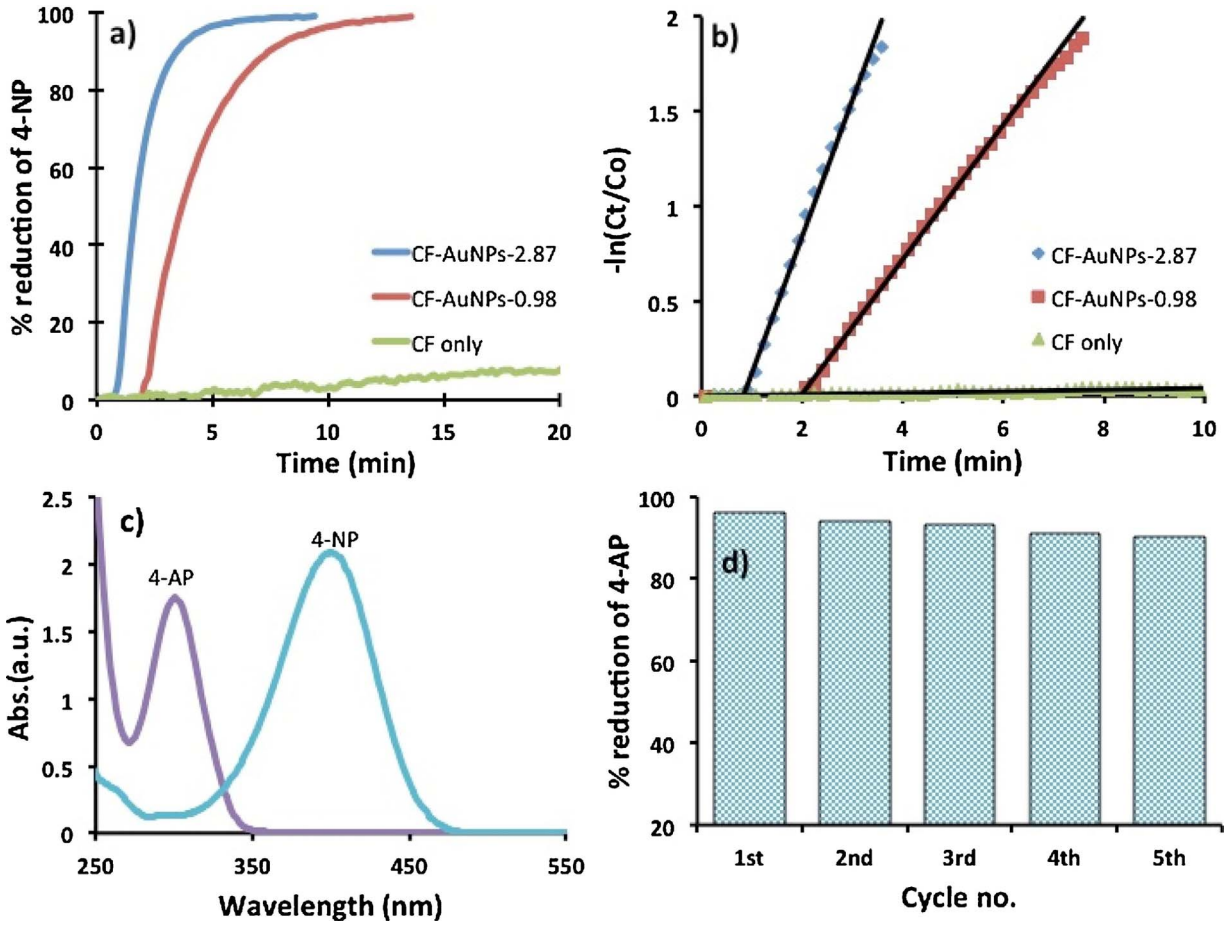


**Fig. 6.** a) Time-dependent reduction of 4-NP into 4-AP, b) Pseudo-first order kinetics of the reactions, and c) UV–vis spectrum of the 4-nitrophenolate (10× diluted) and the 4-AP at the beginning and the end of catalysis, respectively. d) Recyclability of the CF-AuNPs-2.87 towards the reduction of 4-NP.

### *4.2. Catalytic reduction of 4-nitrophenol by the nanocomposites*

The time-dependent percent reduction of 4-NP to 4-AP and the corresponding kinetics of the reactions are shown in Fig. 6a and b, respectively. The $-\ln(C_t/C_0)$ vs time (t) is a straight line, which indicates that the reactions follow pseudo-first order kinetics [44]. The apparent rate constants ($k_{app}$) of the reactions, calculated from the slope of the trendlines, are calculated to be $1.03 \times 10^{-2}\,s^{-1}$, $5.19 \times 10^{-3}\,s^{-1}$ and $6.67 \times 10^{-5}\,s^{-1}$, for the CF-AuNPs-2.87, CF-AuNPs-0.98 and pristine CF, respectively. Compared to the uncatalyzed reaction, where pristine CF was used with $NaBH_4$, the CF-AuNPs-2.87 and CF-AuNPs-0.98 catalyzed reactions are about 154 times and 78 times faster, respectively. The normalized rate constants ($k_{nor}$), obtained by dividing the $k_{app}$ by the amount of AuNPs [45], are calculated to be 35.40 and 52.15 for the CF-AuNPs-2.87 and CF-AuNPs-0.98 respectively. Moreover, it was observed that the CF-AuNPs-2.87 and CF-AuNPs-0.98 catalyzed reactions had induction periods of about 1 min and 2 min, respectively. The induction period is typically observed in heterogeneous catalysis, which is the time it takes to achieve the adsorption and desorption equilibrium between the reactants and the products [46]. The un-catalyzed reaction shows about 8 percent reduction of 4-NP after 20 min of reaction time, which in turn signifies the robust nature of 4-NP to undergo the reduction.

The UV–vis spectrum of the 4-nitrophenolate and its reduced product *viz.* 4-AP is shown in Fig. 6c. It is observed that the absorption band centered at 400 nm, which is the characteristic band for 4-nitrophenolate, diminished after the reduction. However, a new absorption band originated at 300 nm, which is the characteristic band for 4-AP [47,48]. The reduction product *viz.* 4-AP was also characterized by mass spectrometry, which showed strong peak at $m/z = 109$ (Supporting information, Fig. S8).

The stability of the nanocomposite CF-AuNPs-2.87 was also investigated by carrying out the catalytic reduction of 4-NP for five successive cycles, Fig. 6d. The percent reduction of 4-NP was measured after 10 min of catalysis in every cycle. It was observed that the CF-AuNPs-2.87 effectively reduced about 91 percent of the 4-NP to 4-AP on the 5th cycle. Little drop of catalytic activity is also observed from the 1st through 5th cycle. This little loss of activity may have happened because of the gradual loss of the catalyst during the centrifugal separation prior to the use of next cycle.

### *4.3. Catalytic reduction of MO and MB by nanocomposites*

The time-dependent percent reductive decolorization of MO and MB along with their corresponding kinetics of the reduction is shown in Fig. 7. Fig. 7a shows that the reduction of MO catalyzed by CF-AuNPs-2.87 is faster than the one catalyzed by CF-AuNPs-0.98. The reduction follows the pseudo-first order type kinetics, Fig. 7b. The apparent rate constants ($k_{app}$) were found to be $4.58 \times 10^{-3}\,s^{-1}$, $3.36 \times 10^{-3}\,s^{-1}$ and $1.27 \times 10^{-4}\,s^{-1}$, for the CF-AuNPs-2.87, CF-AuNPs-0.98 and pristine CF, respectively.

Likewise 4-NP and MO the reduction of MB catalyzed by CF-AuNPs-2.87 is faster than the one catalyzed by CF-AuNPs-0.98, Fig. 7c. The apparent rate constants ($k_{app}$) were calculated to be $4.82 \times 10^{-3}\,s^{-1}$, $3.99 \times 10^{-3}\,s^{-1}$ and $1.20 \times 10^{-4}\,s^{-1}$, for CF-AuNPs-2.87, CF-AuNPs-0.98 and pristine CF, respectively.

The summary of the catalytic reductions of 4-NP, MO and MB by the CF-supported AuNPs is shown in Table 1. It is observed that the rate of

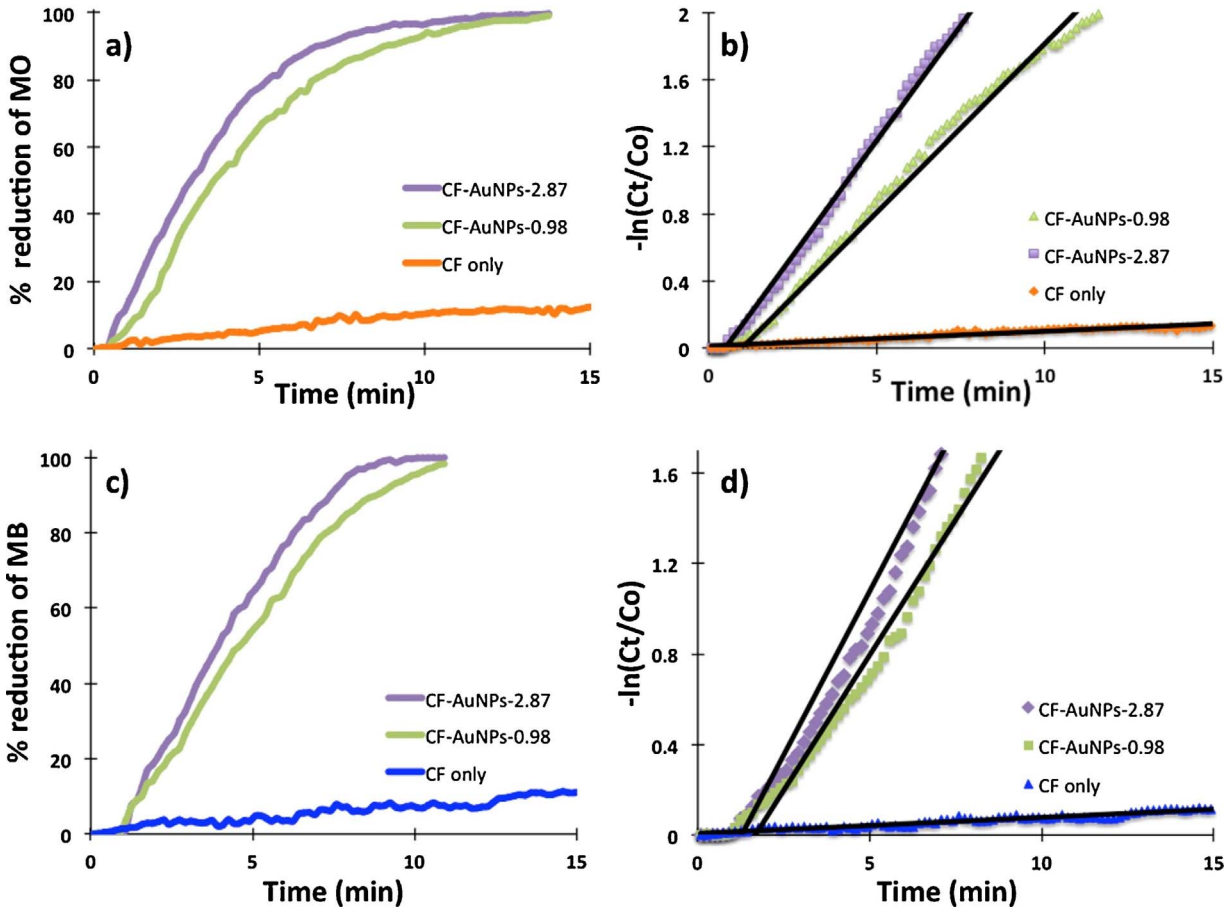


**Fig. 7.** Time-dependent reductive decolorization of a) MO and c) MB. Pseudo-first order kinetics of the reduction of b) MO and d) MB.

reduction depends upon the concentration of AuNPs, provided that the concentration of $NaBH_4$ and the size of the AuNPs remain constant. An increase in the concentration of AuNPs increases the reduction rate and vice-versa. However, the normalized rate constant ($k_{app}$) decreased with the increase in the amount of AuNPs.

### 4.4. Catalytic reduction of 4-NP and MB in tap water

The catalytic activity of CF supported AuNPs towards the reduction of 4-NP and MB in tap water is shown in Supporting information, Fig. S9. The apparent rate constants ($k_{app}$) in the reduction of 4-NP were found to be $1.70 \times 10^{-2}\,s^{-1}$, $1.31 \times 10^{-2}\,s^{-1}$ and $8.67 \times 10^{-3}\,s^{-1}$, for the CF-AuNPs-2.87, CF-AuNPs-0.98 and pristine CF, respectively. The reduction of MB also showed the similar catalytic activity with the apparent rate constants of $6.74 \times 10^{-3}\,s^{-1}$, $6.02 \times 10^{-3}\,s^{-1}$ and $2.68 \times 10^{-3}\,s^{-1}$, for the CF-AuNPs-2.87, CF-AuNPs-0.98 and pristine CF, respectively. The catalytic reduction of both the 4-NP and MB in tap water showed higher values of induction period and higher apparent rate constants compared to those done in deionized water. Moreover, it was found that the tape water by itself showed the catalytic reduction ability unlike the deionized water (Supporting information, Fig. S10). One possible explanation could be the presence of transition metal ions in tap water that may have done the catalysis in presence of $NaBH_4$.

### 4.5. Continuous catalytic reduction of 4-NP, MO, and MB through the reactor column

The performance of the column reactor in the continuous catalytic reduction of 4-NP, MO, and MB is shown in Fig. 8. The freshly prepared solutions of 4-NP, MO and MB with $NaBH_4$ were continuously fed into the column and the UV–vis spectroscopy was taken on the feed and outlet solutions, Fig. 8a–c. The characteristic absorption bands of 4-

**Table 1**
Summary of the catalytic reduction in deionized water.

| Catalysts | Substrates | Amount of AuNPs (mmol) | mol% of AuNPs with respect to substrate | Apparent rate constant $k_{app}$ ($s^{-1}$) | Normalized rate constant $k_{nor}$($s^{-1}$ $mmol^{-1}$) |
|---|---|---|---|---|---|
| CF-AuNPs-2.87 | 4-NP | $2.91 \times 10^{-4}$ | 17.48 | $1.03 \times 10^{-2}$ | 35.40 |
| CF-AuNPs-0.98 | 4-NP | $9.95 \times 10^{-5}$ | 5.96 | $5.19 \times 10^{-3}$ | 52.16 |
| CF only | 4-NP | 0 | 0 | $6.67 \times 10^{-5}$ | – |
| CF-AuNPs-2.87 | MO | $2.91 \times 10^{-4}$ | 16.02 | $4.58 \times 10^{-3}$ | 15.71 |
| CF-AuNPs-0.98 | MO | $9.95 \times 10^{-5}$ | 5.47 | $3.36 \times 10^{-3}$ | 33.77 |
| CF only | MO | 0 | 0 | $1.27 \times 10^{-4}$ | – |
| CF-AuNPs-2.87 | MB | $2.91 \times 10^{-4}$ | 15.72 | $4.82 \times 10^{-3}$ | 16.53 |
| CF-AuNPs-0.98 | MB | $9.95 \times 10^{-5}$ | 5.37 | $3.99 \times 10^{-3}$ | 40.10 |
| CF only | MB | 0 | 0 | $1.20 \times 10^{-4}$ | – |

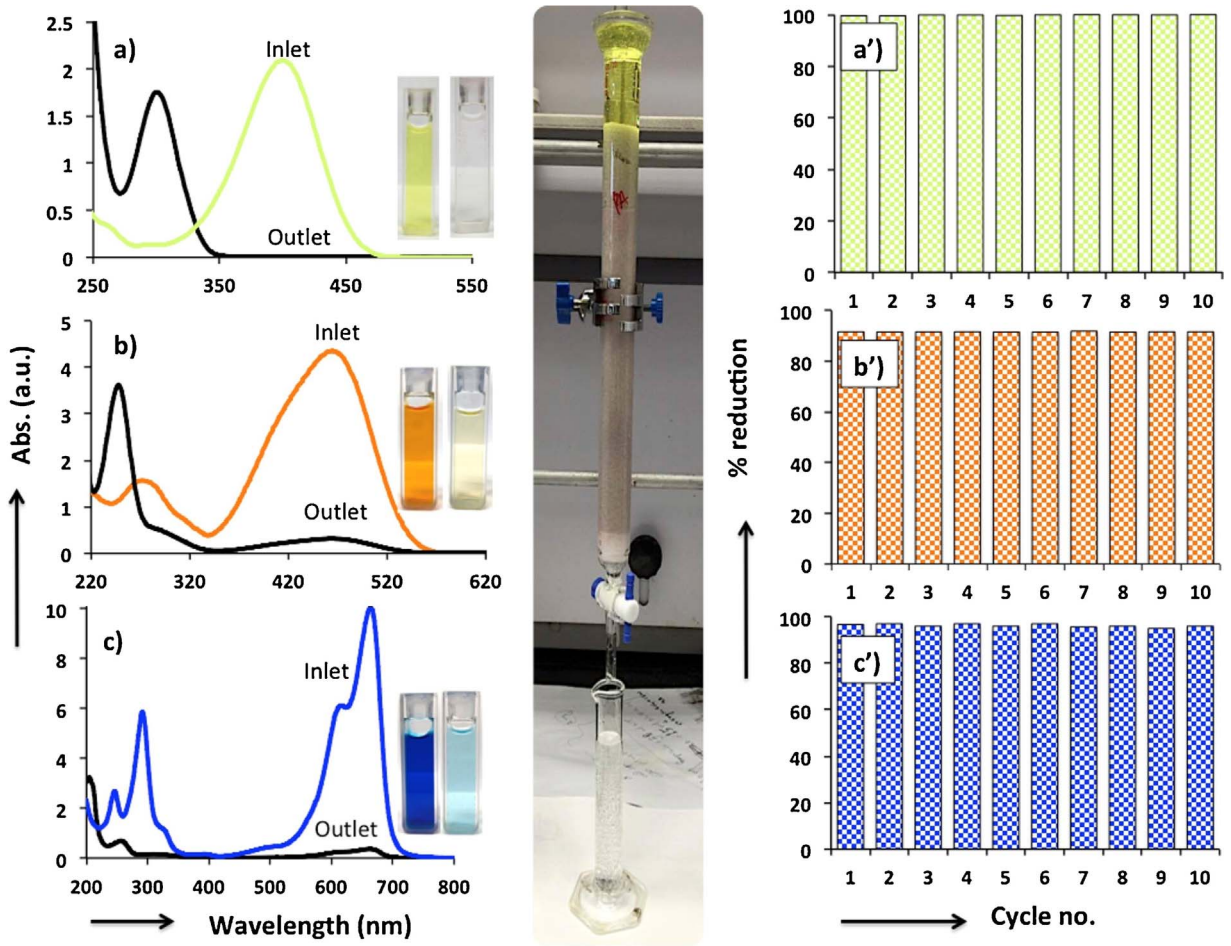


**Fig. 8.** UV–vis spectrum of the inlet and the outlet solutions of a) 4-NP, b) MO and c) MB passed through the column. The reduction of a') 4-NP, b') MO and c') MB for 10 successive cycles. Inset: An operating packed column showing the continuous reduction of 4-NP.

nitrophenolate, MO and MB at 400, 465 and 615 nm, respectively went down significantly with the gradual decolorization of the solutions. Decolorization of 4-NP happens because of the reduction of $NO_2$ into $NH_2$, where $NO_2$ acts as the chromophore. On the other hand, the reductive decolorization of MO and MB happens because of the breaking of the conjugation throughout the backbone of the molecules. New absorption bands were observed at 300, 250 and 256 nm, respectively for the reduction products of 4-nitrophenolate, MO and MB. The reduction product of 4-NP *viz*. 4-AP gives a new characteristic absorption band at 300 nm with the drop of absorption band at 400 nm, which is the characteristic band of 4-nitrophenolate. The reduction product of MO also generates a new absorption band at 250 nm that could be assigned to as the characteristic band for benzene sulfonic acid, which is reported by other researchers [25]. The presence of benzene sulfonic acid along with other degradation species was confirmed by mass spectrometry [49] (Supporting information, Fig. S11). On the other hand, the reduction product of MB *viz.* leucomethylene blue generates a new band at 256 nm in UV–vis spectrum. [50–52] Mass spectrometric analysis further confirmed the presence leucomethylene blue along with other reduction species (Supporting information, Fig. S12).

Fig. 8a'–c' shows the percent reduction of 4-NP, MO and MB, respectively for 10 successive cycles. It was observed that more than 99 percent of the 4-NP was reduced to 4-AP in every cycle. However, in the catalysis of MB and MO the percent reduction observed was about 96 and 92, respectively. This further indicates the efficiency and the cyclic stability of the CF-supported AuNPs towards the reduction of 4-NP, MO and MB.

## 5. Conclusions

In conclusion, we demonstrate sodium rhodizonate as a novel reducing and stabilizing agent for the synthesis of gold nanoparticles and whose size depends on the temperature at which the synthesis is carried out. Sodium rhodizonate-stabilized gold nanoparticles readily bind to cellulose fibers forming stable nanocomposites with high catalytic activity. The nanocomposites exhibited catalytic activity and cyclic stability towards the reduction of 4-nitrophenol and organic dyes such as methyl orange and methylene blue. Moreover, a glass column was packed with the nanocomposites to demonstrate the continuous catalytic reduction of 4-nitrophenol, methyl orange, and methylene blue for multiple cycles.

## Notes

The authors declare no conflicting financial interest.

## Acknowledgments

Financial support from NSF grants CHE-0748913, DMR PREM-1025302, the NEWT-1449500, and USDA2014-38422-22078 are gratefully acknowledged. We thank Jesse Murillo of Dr. Luis Echegoyen research group for his kind assistance with MALDI-MS analysis. We would also like to thank Dr. Jorge Gardea-Torresdey research group for their assistance with DLS and Zeta-potential measurements.

## Appendix A. Supplementary data

Supplementary data associated with this article can be found, in the online version, at http://dx.doi.org/10.1016/j.jece.2017.08.017.

## References


[1] K.A.G. Gusmão, L.V.A. Gurgel, T.M.S. Melo, L.F. Gil, Adsorption studies of methylene blue and gentian violet on sugarcane bagasse modified with EDTA dianhydride (EDTAD) in aqueous solutions: kinetic and equilibrium aspects, J. Environ. Manage. 118 (2013) 135–143.

[2] K.R. Ramakrishna, T. Viraraghavan, Dye removal using low cost adsorbents, Wat. Sci. Tech. 36 (1997) 189–196.

[3] Y. Xie, B. Yan, H. Xu, J. Chen, Q. Liu, Y. Deng, H. Zeng, Highly regenerable mussel-inspired $Fe_3O_4$@polydopamine-Ag coreshell microspheres as catalyst and adsorbent for methylene blue removal, ACS Appl. Mater. Interfaces 6 (2014) 8845–8852.

[4] Ratna, B.S. Padhi, Pollution due to synthetic dyes toxicity & carcinogenicity studies and remediation, J. Environ. Sci. 3 (2012) 940–955.

[5] R.A. Soomro, A. Nafady, Catalytic reductive degradation of methyl orange using air resilient copper nanostructures, J. Nanomater. 16 (2015) 120.

[6] X.C. Jin, G.Q. Liu, Z.H. Xu, W.Y. Tao, Decolorization of a dye industry effluent by Aspergillus fumigatus XC6, Appl. Microbiol. Biotechnol. 74 (2007) 239–243.

[7] V. Vaiano, O. Sacco, D. Sannino, P. Ciambelli, Nanostructured N-doped $TiO_2$ coated on glass spheres for the photocatalytic removal of organic dyes under UV or visible light irradiation, Appl. Catal. B: Environ. 170 (2015) 153–161.

[8] S. Shahabuddin, N.M. Sarih, M. Afzal Kamboh, H. Rashidi Nodeh, S. Mohamad, Synthesis of polyaniline-coated graphene Oxide@$SrTiO_3$ nanocube nanocomposites for enhanced removal of carcinogenic dyes from aqueous solution, Polymers 8 (2016) 305.

[9] S.B. Khan, M. Hou, S. Shuang, Z. Zhang, Morphological Influence of $TiO_2$ Nanostructures (nanozigzag, nanohelics and nanorod) on photocatalytic degradation of organic dyes, Appl. Surf. Sci. 400 (2017) 184–193.

[10] K.B. Narayanan, N. Sakthivel, Synthesis and characterization of nano-gold composite using Cylindrocladium floridanum and its heterogeneous catalysis in the degradation of 4-nitrophenol, J. Hazard. Mater. 189 (2011) 519–525.

[11] K.S. Thangamani, N.M. Andal, E.R. Kumar, M. Saravanabhavan, Utilization of magnetic nano cobalt ferrite doped capra aegagrus hircus dung activated carbon composite for the adsorption of anionic dyes, J. Environ. Chem. Eng. 5 (2017) 2820–2829.

[12] B.H. Tan, T.T. Teng, A.M. Omar, Removal of dyes and industrial dye wastes by magnesium chloride, Water Res. 34 (2000) 597–601.

[13] M. Sayed, L.A. Shah, J.A. Khan, N.S. Shah, J. Nisar, H.M. Khan, P. Zhang, A.R. Khan, Efficient photocatalytic degradation of norfloxacin in aqueous media by hydrothermally synthesized immobilized $TiO_2$/Ti films with exposed {001} facets, J. Phys. Chem. A 120 (2016) 9916–9931.

[14] J. Huang, H. Song, C. Chen, Y. Yang, N. Xu, X. Ji, C. Li, J.A. You, Facile synthesis of N-doped $TiO_2$ nanoparticles caged in MIL-100 (Fe) for photocatalytic degradation of organic dyes under visible light irradiation, J. Environ. Chem. Eng. 5 (2017) 2579–2585.

[15] F. Torrades, M. Pérez, H.D. Mansilla, J. Peral, Experimental design of Fenton and photo-fenton reactions for the treatment of cellulose bleaching effluents, Chemosphere 53 (2003) 1211–1220.

[16] M. Sayed, J.A. Khan, L.A. Shah, N.S. Shah, H.M. Khan, F. Rehman, A.R. Khan, A.M. Khan, Degradation of quinolone antibiotic, norfloxacin, in aqueous solution using gamma-ray irradiation, Environ. Sci. Pollut. Res. 23 (2016) 13155–13168.

[17] Y. Fu, T. Viraraghavan, Fungal decolorization of dye wastewaters: a review, Bioresour. Technol. 79 (2001) 251–262.

[18] O.J. Hao, H. Kim, P.C. Chiang, Decolorization of wastewater, Crit. Rev. Environ. Sci. Technol. 30 (2000) 449–505.

[19] E. Brillas, C.A. Martínez-Huitle, Decontamination of wastewaters containing synthetic organic dyes by electrochemical methods. An updated review, Appl. Catal. B: Environ. 166 (2015) 603–643.

[20] L. Yang, S. Luo, Y. Li, Y. Xiao, Q. Kang, Q. Cai, High efficient photocatalytic degradation of p-nitrophenol on a unique $Cu_2O/TiO_2$ pn heterojunction network catalyst, Environ. Sci. Technol. 44 (2010) 7641–7646.

[21] L.A. Shah, A. Haleem, M. Sayed, M. Siddiq, Synthesis of sensitive hybrid polymer microgels for catalytic reduction of organic pollutants, J. Environ. Chem. Eng. 4 (2016) 3492–3497.

[22] S. Xie, P. Huang, J.J. Kruzic, X. Zeng, H. Qian, A highly efficient degradation mechanism of methyl orange using Fe-based metallic glass powders, Sci. Rep. 6 (2016).

[23] P. Saikia, A.T. Miah, P.P. Das, Highly efficient catalytic reductive degradation of various organic dyes by Au/$CeO_2$-$TiO_2$ nano-hybrid, J. Chem. Sci. 129 (2017) 81–93.

[24] O.A. Zelekew, D.H. Kuo, A two-oxide nanodiode system made of double-layered p-type $Ag_2O$@n-type $TiO_2$ for rapid reduction of 4-nitrophenol, Phys. Chem. Chem. Phys. 18 (2016) 4405–4414.

[25] J. Fan, Y. Guo, J. Wang, M. Fan, Rapid decolorization of azo dye methyl orange in aqueous solution by nanoscale zerovalent iron particles, J. Hazard. Mater. 166 (2009) 904–910.

[26] P.X. Zhao, X.W. Feng, D.S. Huang, G.Y. Yang, D. Astruc, Basic concepts and recent advances in nitrophenol reduction by gold-and other transition metal nanoparticles, Coordin. Chem. Rev. 287 (2015) 114–136.

[27] P. Deka, R.C. Deka, P. Bharali, In situ generated copper nanoparticle catalyzed reduction of 4-nitrophenol, New J. Chem. 38 (2014) 1789–1793.

[28] V.K. Vidhu, D. Philip, Catalytic degradation of organic dyes using biosynthesized silver nanoparticles, Micron 56 (2014) 54–62.

[29] B.K. Ghosh, S. Hazra, B. Naik, N.N. Ghosh, Preparation of Cu nanoparticle loaded SBA-15 and their excellent catalytic activity in reduction of variety of dyes, Powder Tech. 269 (2015) 371–378.

[30] M.L. Wang, T.T. Jiang, Y. Lu, H.J. Liu, Y. Chen, Gold nanoparticles immobilized in hyperbranched polyethylenimine modified polyacrylonitrile fiber as highly efficient and recyclable heterogeneous catalysts for the reduction of 4-nitrophenol, J. Mater. Chem. A 1 (2013) 5923–5933.

[31] S. Eustis, M.A. El-Sayed, Why gold nanoparticles are more precious than pretty gold: noble metal surface plasmon resonance and its enhancement of the radiative and nonradiative properties of nanocrystals of different shapes, Chem. Soc. Rev. 35 (2006) 209–217.

[32] H.S. Devi, N.R. Singh, H.P. Singh, T.D. Singh, Facile synthesis of biogenic gold nanocatalyst for efficient degradation of organic pollutants, J. Environ. Chem. Eng. 3 (2015) 2042–2049.

[33] N. Pradhan, A. Pal, T. Pal, Catalytic reduction of aromatic nitro compounds by coinage metal nanoparticles, Langmuir 17 (2001) 1800–1802.

[34] J. Liu, G. Qin, P. Raveendran, Y. Ikushima, Facile green synthesis, characterization, and catalytic function of β-D-glucose-stabilized au nanocrystals, Chem. Eur. J. 12 (2006) 2131–2138.

[35] J. He, T. Kunitake, A. Nakao, Facile in situ synthesis of noble metal nanoparticles in porous cellulose fibers, Chem. Mater. 15 (2003) 4401–4406.

[36] C.M. Lee, J. Gu, K. Kafle, J. Catchmark, S.H. Kim, Cellulose produced by Gluconacetobacter xylinus strains ATCC 53524 and ATCC 23768: pellicle formation, post-synthesis aggregation and fiber density, Carbohydr. Polym. 133 (2015) 270–276.

[37] K. Watanabe, M. Tabuchi, Y. Morinaga, F. Yoshinaga, Structural features and properties of bacterial cellulose produced in agitated culture, Cellulose 5 (1998) 187–200.

[38] M.T. Islam, S.K. Molugu, P.H. Cooke, J.C. Noveron, Fullerene stabilized gold nanoparticles, New J. Chem. 39 (2015) 5923–5926.

[39] M.A. Uppal, A. Kafizas, M.B. Ewing, I.P. Parkin, The room temperature formation of gold nanoparticles from the reaction of cyclohexanone and auric acid; a transition from dendritic particles to compact shapes and nanoplates, J. Mater. Chem. A 1 (2013) 7351–7359.

[40] C.C. Wang, C.T. Kuo, P.T. Chou, G.H. Lee, Rhodizonate metal complexes with a 2D chairlike $M_6$ metal-Organic framework: $[M(C_6O_6)(bpym)(H_2O)]\cdot nH_2O$, Angew. Chem. Int. Ed. 43 (2004) 4507–4510.

[41] A. Vogler, Photoluminescence and photochemistry of $Pt(II)(PPh_3)_2(C_6O_6)$ induced by rhodizonate IL excitation, Inorg. Chem. Commun. 74 (2016) 90–92.

[42] H. Koga, E. Tokunaga, M. Hidaka, Y. Umemura, T. Saito, A. Isogai, T. Kitaoka, Topochemical synthesis and catalysis of metal nanoparticles exposed on crystalline cellulose nanofibers, Chem. Commun. 46 (2010) 8567–8569.

[43] M. Chen, H. Kang, Y. Gong, J. Guo, H. Zhang, R. Liu, Bacterial cellulose supported gold nanoparticles with excellent catalytic properties, ACS Appl. Mater. Interfaces 7 (2015) 21717–21726.

[44] K. Urkude, S.R. Thakare, S. Gawande, An energy efficient photocatalytic reduction of 4-nitrophenol, J. Environ. Chem. Eng. 2 (2014) 759–764.

[45] W. Shen, Y. Qu, X. Pei, S. Li, S. You, J. Wang, Z. Zhang, J. Zhou, Catalytic reduction of 4-nitrophenol using gold nanoparticles biosynthesized by cell-free extracts of Aspergillus sp. WL-Au, J. Hazard. Mater. 321 (2017) 299–306.

[46] S.K. Das, C. Dickinson, F. Lafir, D.F. Brougham, E. Marsili, Synthesis, characterization and catalytic activity of gold nanoparticles biosynthesized with Rhizopus oryzae protein extract, Green Chem. 14 (2012) 1322–1334.

[47] M.T. Islam, J.E. Padilla, N. Dominguez, D.C. Alvarado, M.S. Alam, P.H. Cooke, M.M.J. Tecklenburg, J.C. Noveron, Green synthesis of gold nanoparticles reduced and stabilized by squaric acid and supported on cellulose fibers for the catalytic reduction of 4-nitrophenol in water, RSC Adv. 6 (2016) 91185–91191.

[48] S. Panigrahi, S. Basu, S. Praharaj, S. Pande, S. Jana, A. Pal, S.K. Ghosh, T. Pal, Synthesis and size-selective catalysis by supported gold nanoparticles: study on heterogeneous and homogeneous catalytic process, J. Phys. Chem. C 111 (2007) 4596–4605.

[49] M.U.D. Sheikh, G.A. Naikoo, M. Thomas, M. Bano, F. Khan, Solar-assisted photocatalytic reduction of methyl orange azo dye over porous $TiO_2$ nanostructures, New J. Chem. 40 (2016) 5483–5494.

[50] U. Kurtan, M. Amir, A. Yıldız, A. Baykal, Synthesis of magnetically recyclable $MnFe_2O_4$@ $SiO_2$@Ag nanocatalyst: its high catalytic performances for azo dyes and nitro compounds reduction, Appl. Surf. Sci. 376 (2016) 16–25.

[51] T.J.I. Edison, M.G. Sethuraman, Instant green synthesis of silver nanoparticles using Terminalia chebula fruit extract and evaluation of their catalytic activity on reduction of methylene blue, Process Biochem. 47 (2012) 1351–1357.

[52] Y. Jiang, S. Zhang, Q. Ji, J. Zhang, Z. Zhang, Z. Wang, Ultrathin $Cu_7S_4$ nanosheets-constructed hierarchical hollow cubic cages: one-step synthesis based on Kirkendall effect and catalysis property, J. Mater. Chem. A 2 (2014) 4574–4579.